IEEE Transactions on ULTRASONICS

Adaptive Transcranial Ultrasound Doppler Imaging of the Brain

Rick Waasdorp, Eleonora Muñoz-Ibarra, Flora Nelissen, Baptiste Heiles, Valeria Gazzola, David Maresca, and Guillaume Renaud

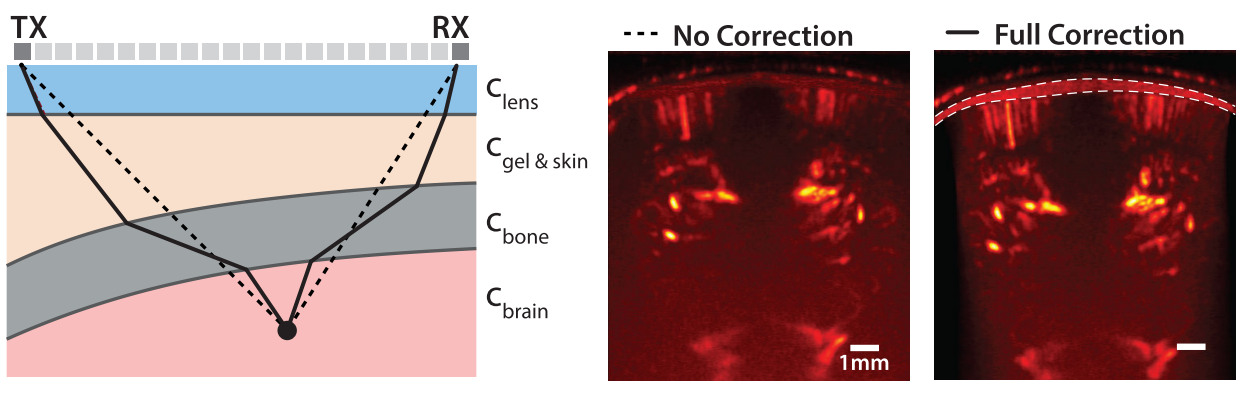

***Abstract*—The development of fully noninvasive, transcranial functional ultrasound (fUS) would increase the translatability and clinical potential of this neuroimaging modality. Unfortunately, transcranial fUS is hindered by skull-induced aberrations which degrade the power Doppler image quality and lower sensitivity. As a result, a majority of fUS imaging studies rely on craniotomies or acoustically transparent cranial windows. To advance fUS technology further, we present an adaptive aberration correction method based on ray-tracing through four tissue layers (transducer lens, gel and skin, bone, and brain tissue). Our method segments these layers and estimates ultrasound wave speeds in each layer iteratively. Once a velocity model of the imaging plane of interest is retrieved, ultrafast power Doppler imaging of the brain is performed using a ray-tracing beamformer that accounts for wave refraction. We tested our method in three adult rats, and estimated wave speeds for the skin/gel layer (1628 ± 7 m/s), skull bone (3247 ± 110 m/s), and brain tissue (1526 ± 55 m/s). After aberration correction, we measured an average adult rat skull thickness of 388 ± 41 μm in agreement with anatomical records. The largest improvements in the Doppler imaging quality were observed in cortical brain layers adjacent to the skull; specifically, lateral spatial resolution was improved by 32%. Our method consistently outperformed Doppler imaging based on traditional delay-and-sum (DAS) beamforming, which assumes a uniform sound speed.**

Received 28 November 2025; accepted 15 March 2026. Date of publication 18 March 2026; date of current version 7 July 2026. This work was supported in part by the Medical Delta Ultra HB Program (RW); in part by the Chan Zuckerberg Initiative (Dynamic Imaging) under Grant 2023-321233, EMI; in part by European Union's Horizon 2020 Research and Innovation Program, ERC-StG "HelpUS" under Grant 758703 (FN, VG); in part by European Union (Marie Skłodowska-Curie Fellowship) under Grant MIC-101032769, BH; and in part by the 4TU Precision Medicine Program (DM). *(Guillaume Renaud and David Maresca are co-last authors.) (Corresponding authors: Guillaume Renaud; David Maresca.)*

This work involved animals in its research. Approval of all ethical and experimental procedures and protocols was granted in part by the Dutch Central Authority for Scientific Procedures under Application No. AVD8010020209725 and in part by the Welfare Body at the Netherlands Institute for Neuroscience under Application No. NIN21.36.02.

Please see the Acknowledgment section of this article for the author affiliations.

Digital Object Identifier 10.1109/TUSON.2026.3675441

I. Introduction

FUNCTIONAL ultrasound (fUS) has emerged as a valuable imaging modality for detecting cerebral blood volume variations associated with neural activity [1], [2]. fUS stands out for its portability, sensitivity, and spatiotemporal resolution compared with the functional magnetic resonance imaging [3]. Clinically, fUS has been used at bedside to monitor neonate health [4] and intraoperatively in adults during tumor resection surgeries [5], [6], [7]. fUS allows analysis of cerebral hemodynamic signals on a signal-trial basis, making transient neural activity detectable [8]. These capabilities led to the decoding of movement intentions in nonhuman primates, which represented a fundamental step toward the development of ultrasound brain–computer interfaces [9]. In spite of these advances, the skull remains a

Highlights

- **We introduce an adaptive four-layer ray-tracing aberration correction method that estimates sound speeds for transcranial ultrasound and improves transcranial power Doppler image quality.**
- **Our method improved lateral resolution in transcranial power Doppler imaging of the adult rat cortex by 32%.**
- **These findings pave the way for noninvasive fUS of the brain, increasing spatial specificity and advancing fUS toward broader clinical and neuroscience applications.**

***Index Terms*— Aberration correction, brain imaging, noninvasive, ray tracing, sound speed estimation, transcranial, ultrasound.**

highly attenuating and aberrating barrier for ultrasound waves that prevents the development of fully noninvasive fUS and the wider adoption of this technology.

The skull bone has a high density and speed of sound (typically 3000 m/s) compared with soft tissues (skin 1600 m/s and brain 1570 m/s) [10]. As a result, transcranial ultrasound images are degraded by several physical effects including multiple scattering, mode conversion [11], absorption [12], and refraction [13] [see Fig. 1(a) and (b)]. This currently restricts the use of fUS in adult humans to intraoperative procedures [7] or chronically implanted acoustic transparent windows [14]. Transcranial fUS is feasible in mice and young rats due to the relatively thin skull [15], [16], but as animals age, and the skull develops [17], other solutions are needed.

Most studies simply remove [1] or thin the skull [18] to prevent aberration, a procedure not compatible with clinical fUS or fUS-based brain–machine interfaces. As an alternative to surgical procedures on the skull, the echogenicity of vascular signals can be enhanced using contrast agents [19]. However, the effect is transient due to the gradual elimination of the agent, requiring continuous administration for sustained enhancement. In addition, contrast agents introduce random fluctuations to the functional signal, likely due to variability in microbubble size and concentration per voxel [19], [20]. Therefore, transcranial fUS needs to resort to other methods to overcome skull-induced aberrations.

Alternative to addressing the attenuation problem, the loss of focus can be restored by aberration correction techniques [21]. Most techniques rely on near-field phase-screen modeling [22], where the aberrating layer is modeled as a thin phase screen located at the transducer surface. The phase aberration is corrected by finding the delays to apply to each transducer element, typically by maximizing the correlation between elements [23], maximizing spatial coherence [22], or maximizing speckle brightness [24]. This method can be used in the presence of either bright reflectors such as microbubbles [25], [26], [27] or diffuse scatterers [28]. However, near-field phase-screen methods do not restore positional errors and the aspect ratio of the image [29] and have limited success in strongly aberrating media such as the skull without contrast agents.

Another class of aberration correction methods uses tomography to estimate the speed of sound map of the medium, and uses this to compute the aberrated time of flights through the medium [30], [31], [32]. Although these methods can account for refraction in image reconstruction by using Eikonal solvers, the tomographic wave-speed estimation is performed without accounting for refraction [32]. In addition, these methods have been demonstrated in low-contrast wave speed, and the methods do not handle sharp transitions in wave-speed values as found in transcranial imaging.

Other methods such as ultrasound matrix imaging [33], [34], or deep-learning-based aberration correction [35], [36] have been developed, but these methods currently still require either contrast agents or have been demonstrated in weak aberrating conditions.

Finally, there are methods that employ a layered tissue velocity model to compute the refracted wave path and correct for phase aberration. This requires wave speeds for every tissue layer and an accurate delineation. The skull shape and wave speed can be obtained by ultrasound imaging [37], [38], [39] or by using other imaging modalities such as computed tomography (CT) [40], [41], [42]. However, relying on other imaging modalities has the drawback of potentially introducing co-registration errors and the need for additional costly imaging systems. Once a complete sound speed map is obtained, the propagation of a wavefront through the medium can be computed using the Eikonal equation, and the aberration-corrected time of flights are obtained. The Eikonal equation can be solved using the fast marching method [43]. This has been used in simulation, phantoms [42], [44], [45], and ex vivo human skull [37], [46]. Alternatively, the refracted wave path can be found using two-point ray-tracing [47], allowing imaging of the bone cortex [38], [39], and ex vivo human skull imaging [46]. The aberrated delays can be computed for every source–receiver pair, and finally be used in delay-and-sum (DAS) beamforming [48].

Here, we present an adaptive transcranial ultrasound imaging method to estimate the rat skull geometry and wave speed, and correct for wave refraction in transmission and reception using ray tracing. This method estimates the wave speed for each tissue layer, in the presence of high-contrast wave-speed values between layers and finally correct skull-induced aberrations. The method is contrast agent-free and only requires ultrasound measurements. We validate the method with in vitro experiments with known ground truth and finally evaluate the performance of our approach in transcranial Doppler imaging of adult rat brains.

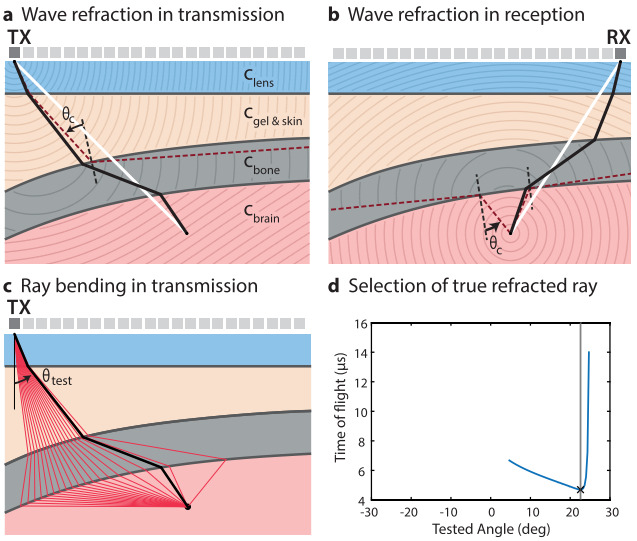

Fig. 1. Wave refraction during transcranial ultrasound imaging. (a) Wave propagation in transmission and (b) reception, through four layers with distinct sound speeds: the transducer lens, acoustic coupling gel and skin tissue, the skull bone, and finally brain tissue. White lines show the wave path in conventional image reconstruction assuming homogeneous wave speed. Black lines show the refracted path through the medium, fulfilling Snell's law. Isophase lines (wavefront) in each layer are spaced at one wavelength λ in water. The dark red dashed lines indicate the paths subject to total internal reflection due to the critical angle θ_c. (c) Ray bending to find the refraction-corrected path through the four-layer model. Ray bending is computed by minimizing the time of flight between source and pixel point or receiver and pixel point, following Fermat's principle. By testing different emerging angles, constructing the path to the pixel, and computing the time of flight, the path fulfilling Snell's law is found by minimizing the time of flight. (d) Time of flight for different tested ray angles illustrated in (c).

II. Methods

A. Aberration Correction Method

In transcranial imaging, the homogeneous wave-speed assumption fails. The skull bone has a significantly higher wave speed than the soft tissues, and therefore, DAS overestimates time of flight and does not account for wave refraction [see Fig. 1(a)]. To obtain the accurate time of flights, we used an adaptive aberration correction method that estimates the wave speed in four tissue layers and corrects the time of flight by retrieving the refracted wave path through ray tracing [see Fig. 1(b)].

The method is divided into three reconstruction steps. In the first step, we use a two-layer model to correct lens refraction, which allows us to accurately estimate the wave speed in the gel/skin layer by autofocusing [49], and segmentation of the outer skull surface. In the second step, we use a three-layer model to estimate the wave speed of the skull bone and segment the inner skull surface. During the final step, we use a four-layer model to estimate the wave speed in the brain tissue and perform the final aberration correction. A graphical overview of the method is shown in Fig. 2.

1) Transducer Parameters: Acoustic Lens and Time to Peak: A prerequisite to all aberration corrections reported in the rest of the article is to characterize the lens and waveform parameters of the transducer. We transmitted a one-cycle imaging pulse in air in a synthetic aperture (SA) sequence and received the internal lens reflections. Then, we found the time to peak, lens thickness, and lens wave speed by maximizing the coherence of the internal lens reflections as described in [49].

2) Four-Layer Velocity Model: The first layer models the transducer lens and allows accounting for refraction at the lens interface. The second layer models both the acoustic coupling gel and skin tissue. The heterogeneity within this layer is assumed to be small, since the ultrasound gel used for coupling is matched with skin tissue in terms of acoustic impedance. The skin wave speed is reported to be 1600–1620 m/s, slightly higher than soft tissue [10], [50].

The third layer in our model represents the skull bone, characterized by its high density and a reported wave speed ranging from 2400 to 3500 m/s [51], [52], [53]. The thickness and curvature of the skull vary considerably, with the supraoccipital bone at the back measuring between 0.6 and 1.2 mm, and the parietal bone in the middle ranging from 0.2 to 0.6 mm, mainly depending on the body mass [54]. Rat skulls consist of plates that grow together and are connected by sutures. The speed of sound in the skull increases with age due to changes in the mineral content of the cortical bone. The sutures consist of collagen-rich connective tissues with sound speeds closer to soft tissue. The skull bone is not a uniform layer but rather a sandwich structure consisting of an outer and inner cortical layers with diploë in between. The diploë is a spongy trabecular bone layer and typically constitutes about one-fifth of the total skull thickness [55], [56]. Given that the diploë layer is too thin to resolve using ultrasound imaging and accounts for a small thickness fraction, we simplify the skull as a single homogeneous layer in our ray-tracing model. The varying curvature and thickness are modeled by segmenting the outer and inner surfaces using piecewise cubic splines.

The final layer models the brain tissue. There is no literature-reported value for the wave speed in rat brain tissue at high frequency and in vivo temperatures. In fresh ex vivo canine brain samples, the wave speed was reported to be between 1563 and 1570 m/s [57], [58], measured at 37 °C and 5 MHz, slightly higher than the averaged soft tissue value of 1540 m/s. We expect the rat brain wave speed to be in the same range.

3) Adaptive Ray Tracing: To find the aberrated round-trip time of flight, we use a ray-tracing method adapted from Renaud et al. [38] that finds the refracted wave path in the four-layer model. The estimated time of flight is used in conventional DAS beamforming to reconstruct the corrected image [48].

The refracted path is found by two-point ray tracing, a technique that is commonly used in seismic imaging [47]. In this technique, Snell's law of refraction is imposed on all but the last interface. The aberrated wave path is found by minimizing the time of flight between a source and pixel point or receiver and pixel point, following Fermat's principle. Specifically, for each source and pixel combination, we test different emerging ray angles from the source, traverse the layers by computing the refracted ray at each interface intersection, except for the last [see Fig. 1(c)]. The last interface intersection point is connected to the endpoint, to compute a time of flight for the tested angle [see Fig. 1(d)]. Finally, we find the path fulfilling

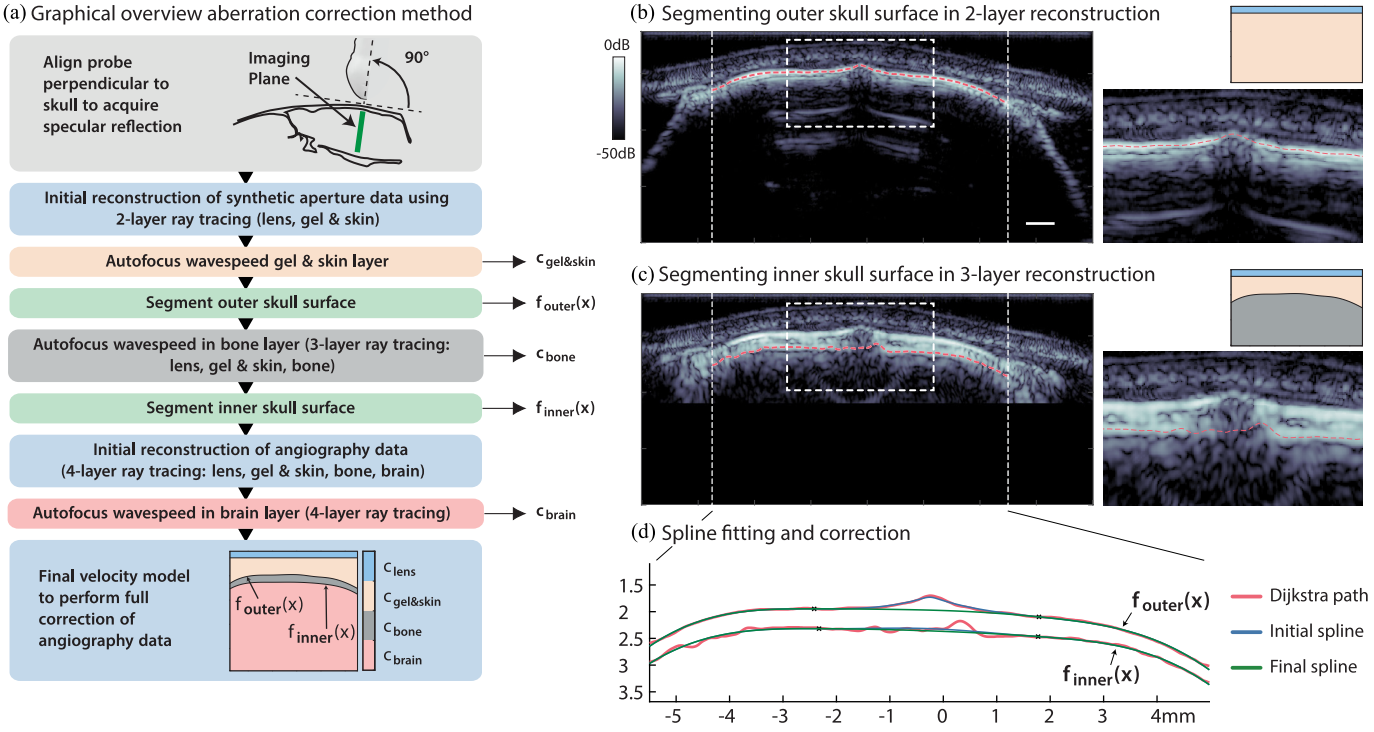

Fig. 2. Overview of the adaptive aberration correction method. (a) Flowchart of method. (b) Outer skull surface segmentation in two-layer model reconstructed B-mode. In the center, the suture causes a protrusion in the retrieved path of maximum brightness (red line). The protrusion has less echogenicity than the rest of the skull surface and is therefore smoothed out in the final spline used in the ray tracing. (c) Inner skull surface segmentation in three-layer model reconstructed B-mode. In the center, there is no clear specular reflection from the inner skull surface. This leads to uncertainty in the path of maximum brightness (red line). This uncertainty is smoothed out in the final spline used in the ray tracing. (d) Spline fitting procedure for both skull surfaces. Dijkstra's algorithm is used to find the path of maximum brightness (red line), to which a piecewise cubic spline with is fit (blue line). To remove the section in the center, we found the breakpoints on the spline (black crosses), and fit new cubic spline sections between these points. Resulting in the final smooth and continuous spline (green line). In (b) and (c), white dashed lines indicate the field of view that was chosen for all subsequent processing.

Snell's law by minimizing the time of flight using Brent's algorithm [59]. This process is repeated for all combinations of sources and pixel points and receivers and pixel points. The algorithm gives access to the reception angle for each source–pixel–receiver combination, which is used to account for element directivity in the beamforming process [60].

A MATLAB (MathWorks, Natick, MA, USA) implementation of the ray-tracing algorithm with demonstration is available on GitHub (`https://github.com/MarescaRenaudLabs/us-ray-tracing`). The demo shows how to find the refracted wave path and time of flight through a multilayered medium for a single source–pixel–receiver triplet. The MATLAB demo is not optimized for speed and is intended for educational purposes. The final ray-tracing algorithm used in this article is implemented in C++ and parallelized using OpenMP.

4) Skull Segmentation: To segment the skull, the images were reconstructed with an isotropic pixel size of $\lambda/4$. We then applied a path-finding algorithm, based on Dijkstra's method, to identify the lateral path from left to right through the image that maximizes brightness. The algorithm evaluates all possible pixel connections between neighboring columns and iteratively constructs the path with the highest cumulative brightness across the image. The resulting path was smoothed with a three-sample moving average filter and subsequently fit with a piecewise cubic spline. We choose eight knots to balance the flexibility and smoothness of the spline fit, and the computational complexity of the ray-spline intersection algorithm described in Section II-A5.

In segmentation of the outer bone surface, we noticed that the suture in the center of the skull was protruding upward [see Fig. 2(b)], which introduced downstream artifacts in the reconstruction. Since the suture has a lower speed of sound, we opted to omit this protrusion in the segmentation. To do this, we determined the breakpoints in the piecewise cubic spline on both sides of the suture and fit a new continuous cubic spline between the two breakpoints, effectively smoothing out the suture protrusion. We determined the breakpoints as the zero crossings of the second derivative of the spline. The path, initial spline, and final smoothed spline are shown in Fig. 2(d).

To segment the inner bone surface, we found the lateral path that maximizes brightness below the outer bone surface, using the same path-finding algorithm. Due to the suture, there was no clear specular reflection of the inner bone surface in the center of the image [see Fig. 2(c)]. We fit a piecewise cubic spline to the segmented path, and used the same approach as for the outer bone surface to smooth out the spline in the center of the image below the suture [see Fig. 2(d)].

It proved challenging to segment the skull bone across the full aperture of the transducer due to poor specular reflection of the skull bone at the edges of the image. Even if it was

possible to trace a path for the outer surface, the absence of a clear inner bone surface reflection on the side of the image made it impossible to segment the inner surface [see Fig. 2(c)]. Therefore, we opted to reduce the field of view in the reconstructions to the part where we observed clear specular reflections from both skull surfaces. This typically corresponded to a lateral field of view of approximately 10 mm.

5) Intersection of Rays With Interfaces: During the minimization, the speed of sound map is traversed by rays with different angles. This requires finding the intersection points of a ray with the lens and skull surfaces. The intersection point on the lens surface follows from the tested ray angle and the lens thickness. The intersection point of the refracted ray with the outer skull surface is found by a line-spline intersection algorithm.

To find the intersection point of the ray and the piecewise cubic spline, we need to find in which subdomain the intersection point lies. This is done by testing the ray against all spline segments with potential intersections.

For a ray described by $z = px + q$, and a cubic spline section $z = ax^3 + b\,x^2 + c\,x + d$, we find their intersection point by computing the roots of the equation

$$ax^3 + bx^2 + (c - p)x + (d - q) = 0. \tag{1}$$

This cubic is reduced to a depressed cubic equation of the form

$$t^3 + pt + q = 0. \tag{2}$$

Finally, we apply Cardano's formula to find only the real roots [61]. We obtain one root if the discriminant is positive and three otherwise. Next, we need to test if the found roots are in the domain of the current spline segment. The root is discarded if it is not in the domain; otherwise, we find the intersection point by evaluating the line equation at the root. If no valid real roots are found for a spline segment, the next segment is tested. If no valid roots are found for any segment, the ray does not intersect the spline.

6) Wave-Speed Estimation: We find the wave speed in each layer by autofocusing, in which we reconstruct a region of interest (ROI) of the aberrated image with different wave speeds and select the wave speed that maximizes the image sharpness. Image sharpness is defined by the Brenner gradient

$$F_{\text{Brenner}} = \sum_{x,y} \left(I_{x+2,y} - I_{x,y}\right)^2 + \left(I_{x,y+2} - I_{x,y}\right)^2 \tag{3}$$

where $I_{x,y}$ is the image intensity at location (x, y) [62].

The wave speed in the gel/skin layer is found by using the two-layer model on the SA data from the skull-segmentation sequence. After an initial reconstruction at 1600 m/s, we define ROI 1 around the skull bone [see Fig. 3(d)] and autofocus.

Second, the wave speed in the skull bone is found using the three-layer model. We define ROI 2 around the bone [see Fig. 3(d)] and maximize the sharpness of the inner skull surface. To avoid the influence of the outer bone surface during maximization of the sharpness, a mask that mutes the outer bone surface is applied. After obtaining the wave speed of the skull bone, we can reconstruct a high-resolution B-mode of the total skull and segment the inner skull surface.

To estimate the final missing velocity in the four-layer model, we use the data from the brain angiography sequence. We reconstruct the brain using the four-layer model and an initial wave speed of 1540 m/s, and form the power Doppler image. In this image, we define a ROI around the brain vasculature [see Fig. 4(g)], and autofocus the ROI to maximize the sharpness of the power Doppler images. We use the power Doppler image to autofocus since the SA image has too low signal-to-noise ratio (SNR). Instead, we could have used the B-mode of the brain angiography sequence, but the presence of multiple reflections of the skull biases the autofocusing. Finally, we use the fully characterized four-layer model to reconstruct the full aberration-corrected brain angiographic image.

During the autofocusing process for brain tissue, the vascular content within the ROI changes depending on the tested wave speeds, which biases the focus quality metric. To mitigate this effect, the bounding box of the ROI was shifted by

$$\Delta z = \left(z_{\text{ROI,center}} - z_{\text{skull}}\right) \frac{c_{\text{test}} - c_{\text{center}}}{c_{\text{center}}} \tag{4}$$

with $z_{\text{ROI,center}}$ being the depth of the center of the ROI for autofocusing, z_{skull} being the depth of the inner skull surface at the center of the image, c_{test} being the wave-speed tested, and c_{center} being the mean value of the tested wave speeds.

B. Experimental Methods

1) Phantom Validation: To validate our adaptive aberration correction technique, we estimated the wave speed of three distinct layers in a phantom setup. We submerged a wire phantom with three nylon wires with a diameter of 10 μm in a tank with degassed water [see Fig. 3(a)]. We positioned a 300 $\pm$ 10-μm PVC aberrating layer above the wires (measured with caliper; Mitutoyo, Kawasaki, Japan). The phantom was imaged using the skull segmentation and brain Doppler sequences. Before and after imaging, the water temperature was measured using a high accuracy thermometer with an accuracy of 0.04 °C (PT100 thermocouple, Greisinger Electronics, Germany).

After imaging, we first autofocused the layer of water between the transducer and PVC using the two-layer model, then used the three-layer model to find the wave speed in the PVC and finally used the four-layer model on the plane-wave (PW) data to estimate the wave speed in the water around the wires. The temperature of the water was converted to the ground-truth sound speed of the water using a calibration curve [63]. When the ultrasound estimated thickness of the PVC layer and the wave speed of the water in the third layer match the ground truth, our method is validated.

2) Animal Procedures: Three adult male Sprague Dawley rats were imaged in this study (6–8 weeks old; 260–360 g; Janvier Labs, France). Animals were socially housed in groups of 2–3 in a 12 h reversed light-dark cycle and had ad libitum access to food and water. All experiments were approved under CCD license number AVD8010020209725 and performed at the Netherlands Institute for Neuroscience.

All ultrasound recordings were performed under anesthesia. Prior to imaging, the rats were anesthetized using 5% isoflurane in an induction chamber and then transferred to an inhalation mask with 3% isoflurane for depilating over the head. Next, the rats were placed on a heating pad set to 37 °C, and head-fixed in a stereotactic frame attached to an inhalation mask, delivering 1.5% isoflurane to maintain anesthesia. After positioning the rat in the imaging setup, anesthesia was transitioned from 1.5% isoflurane to medetomidine (0.1 mg/mL) via a single bolus injection. Three minutes later, isoflurane administration was discontinued, and deep anesthesia was confirmed by the absence of a toe pinch reflex. Subsequently, a continuous subcutaneous infusion of medetomidine (0.05 mg/mL) was initiated to maintain anesthesia throughout the imaging session. Centrifuged ultrasound gel (Ultrasonic 100, Parker Laboratories, Orange, NJ, USA) was applied to couple the scalp to the probe. The maximum duration of the experiment was 1.5 h.

C. Ultrasound Acquisitions

Ultrasound acquisitions were performed with a L6-24-D transducer (192 elements; 135 $-\mu$m pitch; GE HealthCare, Chicago, IL, USA) connected to a programmable ultrasound scanner (Vantage 256 High frequency configuration, Verasonics, Kirkland, WA, USA).

Our aberration correction method requires an accurate segmentation of the skull bone. To this end, we implemented a high-resolution skull-segmentation sequence that relies on SA imaging with elementwise transmissions [64]. To obtain the best axial resolution, we transmitted short single-cycle sine-bursts centered at 13.9 MHz.

After bone image acquisition, we switched to PW imaging to acquire ultrafast power Doppler images. We transmitted three cycles sine-bursts centered at 13.9 MHz and 26 PWs ranging from $-5°$ to 5°, resulting in 700-Hz frame rate after coherent compounding [65]. We set the duration of frame ensembles to 250 ms to capture a full-cardiac cycle of the rat in each Doppler image.

To correct for refraction effects in the skull bone, the inner and outer skull interfaces must be clearly resolved in the B-mode image. This requires to position the probe perpendicular to the skull surface to obtain specular echoes from both skull interfaces (see Fig. 2). We used live B-mode imaging to find maximal specular reflections from outer and inner skull interfaces. The probe was positioned 2 mm above the skull surface. Next, we acquired an ultrafast power Doppler image in the same plane using the PW sequence described previously.

We used a real-time DAS beamformer implemented in CUDA on a GPU (GeForce RTX 3090, NVIDIA, Santa Clara, CA, USA) for live display. After beamforming, power Doppler images were formed by separating blood signals from tissue signals using a singular value decomposition (SVD) spatiotemporal clutter filter [66]. Since motion is minimal in head-fixed anesthetized experiments, we used a fixed threshold and removed the first 20% of singular vectors (35 out of 175 frames). RF data from both skull segmentation and brain angiography sequences were saved and processed offline.

D. DAS Beamforming

The most prevalent ultrasound image reconstruction method is DAS beamforming. For each pixel point, the time of flight of the ultrasound wave is calculated for each combination of transmitting and receiving elements. In conventional DAS, the medium is assumed to have a homogeneous sound speed c_0 of 1540 m/s and straight paths are assumed between the source, pixel point and receiver [see Fig. 1(a)]. The image magnitude $s(\vec{x}_p)$ at pixel point $\vec{x}_p$ is given by

$$s(\vec{x}_p) = \sum_{i=1}^{M} \sum_{j=1}^{N} \mathrm{RF}(t = \tau, i, j) w(\vec{x}_p, j) \tag{5}$$

with M being the number of transmissions, N being the number of receiving elements, RF being the recorded data, τ being the delay for pixel $\vec{x}_p$, transmission i, and receiving element j, and $w(\vec{x}_p, j)$ being a weighting to account for element directivity [60]. Ultrasound scanners usually emit short bursts of sine waves, consisting of a few periods of oscillation at the probe's central frequency. To ensure accurate image reconstruction, it is critical to delay the ultrasound signals to the crest of the envelope of the received waves, i.e., the time to peak t_{ttp} of the envelope of the received waveform [49]. Finally, transducers have a lens to focus the ultrasound beam in the elevation plane. Lenses typically have a lower sound speed than soft tissue, and the difference in sound speed has to be accounted for. An estimation for the time to peak and the lens correction term is often given by transducer manufacturers.

To evaluate the aberration correction approach, we reconstructed reference images using the conventional DAS beamforming method with a homogeneous sound speed of 1540 m/s, manufacturer-reported values for time to peak and lens correction, and a standard binary element weighting using F number 2 [48].

E. Evaluation of Image Quality Improvement

We use three reconstruction approaches to compare the image quality. The reference image has no correction (NC) and relies on conventional DAS, using optimized lens parameters [49]. We compare the reference images to a lens correction image (LC) using the two-layer model, and a full correction (FC) with the four-layer model.

To evaluate the resolution improvement and the ability to resolve more vessels, we analyze the Doppler intensity profile along a line through the cortex. Since vessels rarely exhibit a prominence of at least 6-dB relative to adjacent local minima, the conventional full-width at half-maximum (FWHM) metric is not reliably applicable. Instead, we identify vessels with a minimum peak prominence of 2 dB, and compute their width at the -2-dB level.

To assess whether the improvement of our aberration correction technique varies over imaging depth, we compute the mean value and sharpness of the power Doppler image in three ROIs: cortex, midbrain, and deep [see Fig. 7(a)]. We then determine the improvement with respect to the reference image by computing the ratio for both the magnitude and sharpness of the power Doppler image, of LC and FC over NC. Since in the

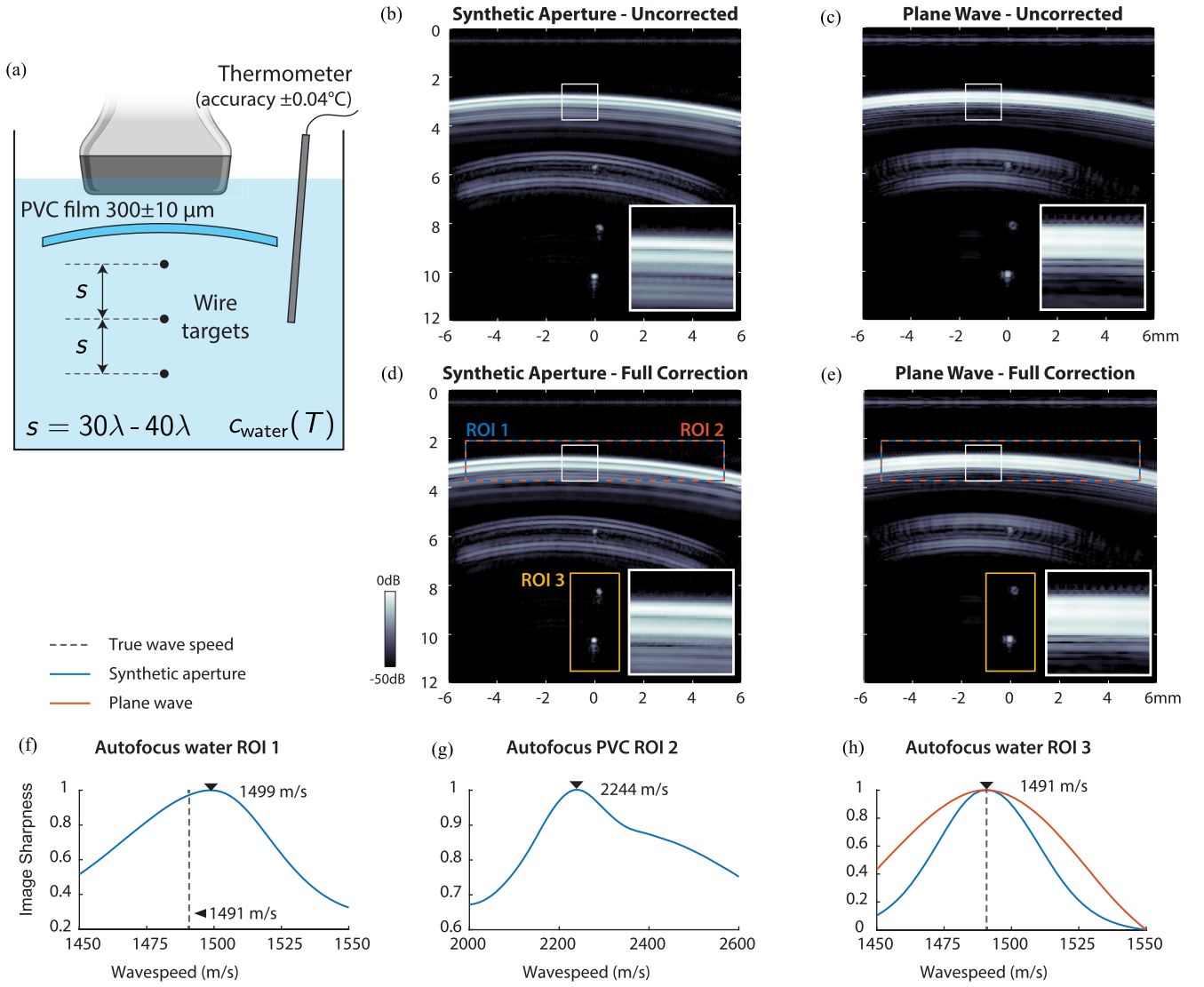

Fig. 3. Aberration correction validation experiment. (a) Phantom validation setup. (b) Uncorrected SA B-mode of the plastic film and wires. (c) Uncorrected PW B-mode. (d) Aberration-corrected SA B-mode. (e) Aberration-corrected PW B-mode. (f) Autofocusing of the first water layer in ROI 1, using the SA data. (g) Autofocusing of the PVC layer in ROI 2, using the SA data. (h) Autofocusing of the last water layer in ROI 3, using both the SA (blue line) and PW (orange line) data.

three reconstruction approaches the skull depth and apparent thickness are different, the ROIs are offset by the difference in apparent skull depth with respect to NC.

To further understand the effect of our aberration correction, we determined the phase aberration law for different points in the image [see crosses in Fig. 7(a)]. The aberration law was found by taking the difference between the return time of flight from the conventional DAS approach and the full correction.

Since the skull is reconstructed with too low a wave speed in the NC and LC images, the bone appears too thin. In addition, the bone layer acts as a diverging lens. When using our four-layer model to correct for the aberrations, this leads to a lateral and axial shift of the brain vasculature in the FC image.

To quantify the thickness of the bone layer, we measured the distance between the outer and inner skull segmentations. We determined the minimum distance of the outer skull segmentation to the inner skull segmentation for every pixel to obtain the skull thickness as a function of lateral position. Finally, we compute the mean skull thickness per subject.

III. Results

In characterizing the transducer, we found a lens wave speed of 1009.6 m/s, a lens thickness of 518.5 μm, and a time to peak of 0.335 μs for the single-cycle waveform and 0.467 μs for the three cycle waveform.

A. Phantom Validation

In the validation experiment, the water temperature was 22.80 °C, corresponding to a wave speed of 1491 m/s [63]. The results of autofocusing for each layer are shown in Fig. 3. The SA imaging sequence was used to estimate wave speeds in the first water and PVC layers, resulting in 1499 and 2244 m/s, respectively. The segmentation of the PVC film revealed a thickness of 290 μm. Finally, autofocusing of the

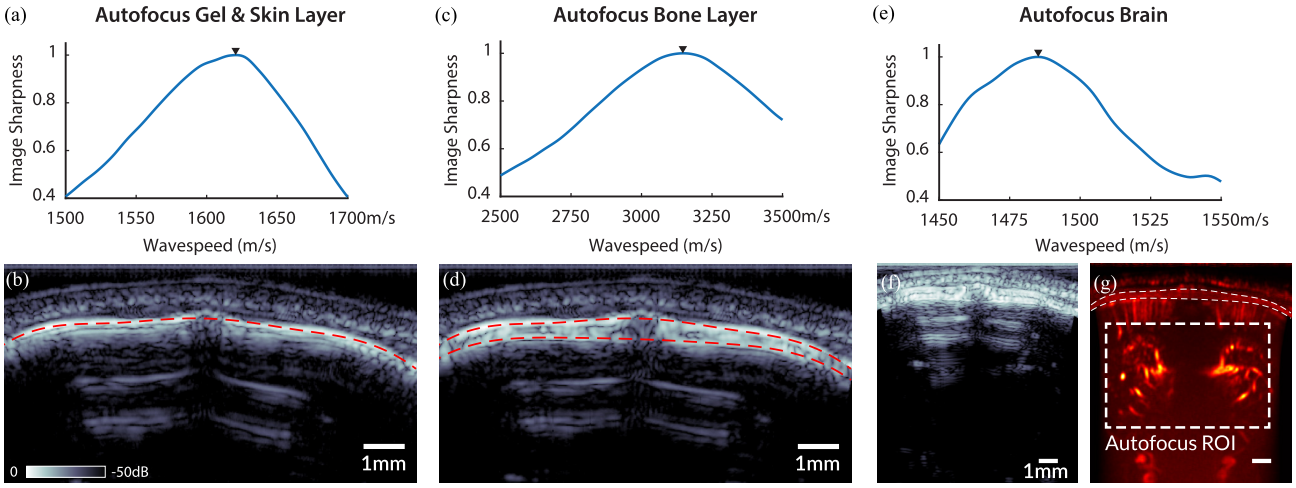

Fig. 4. Wave-speed estimation. (a) Result of autofocusing the gel and skin layer using the SA data. The image is reconstructed using the two-layer model. (b) SA image reconstructed with the estimated wave speed of the gel/skin layer. In this image, the outer skull surface is segmented using Dijkstra's algorithm (red dashed line). (c) Result of autofocusing the skull bone layer using the SA data and the three-layer model. (d) SA image reconstructed with the estimated wave speeds. The inner skull surface is segmented, indicated by the lower red dashed line. (e) Finally, the brain angiography data is used with the four-layer model to autofocus the wave speed in the brain tissue. (f) Aberration-corrected PW B-mode. (g) Power Doppler data to estimate the brain wave speed.

wire targets in the water layer below the PVC film in ROI 3 yielded a wave speed of 1491 m/s for both SA and PW imaging methods. The full aberration-corrected phantom SA image is shown in Fig. 3(d), and the PW image in Fig. 3(e). These findings validate our method's ability to accurately estimate wave speeds and segment layer boundaries of a thin aberrating layer under controlled experimental conditions.

B. Wave-Speed Estimation

Fig. 4 shows the autofocusing curves and step-by-step B-mode images of the rat skull. Fig. 4(a) shows the image sharpness for the tested wave speeds in the gel/skin layer, where we found a mean wave speed of 1628 ± 7 m/s for all rats. Fig. 4(b) shows the lens-corrected SA image of the rat skin and skull with the outer skull surface segmentation. In this image, the bone is reconstructed with a too low wave speed, and shows up with an underestimated thickness. Fig. 4(c) shows the bone autofocusing curve, resulting in a mean wave speed of 3247 ± 110 m/s for all rats. Fig. 4(d) shows the full aberration-corrected SA image of the rat skull, where the inner skull surface is segmented. Compared with the lens-corrected image, the bone is now reconstructed with the correct wave speed and shows up with the correct thickness. The average thickness for all rats was 388 ± 41 μm. Fig. 4(e) shows the autofocusing result for the brain, where we found a mean wave speed of 1526 ± 55 m/s for all rats. Finally, Fig. 4(f) and (g) shows the full aberration-corrected PW B-mode of the rat skull and power Doppler of the brain vasculature. Due to the presence of multiple reflections in the B-mode, we used the shown autofocusing ROI in the power Doppler to retrieve the brain wave speed. The results of the wave speed estimation and segmentation for each rat are shown in Table I.

TABLE I
AGE, WEIGHT, THE RESULTS OF AUTOFOCUSING FOR ALL LAYERS, AND THE MEAN±SD SEGMENTED SKULL THICKNESS FOR EACH RAT

Rat	Age (days)	Weight (g)	Wave speed (m/s) Skin/Gel	Bone	Brain	Thickness skull (μm)
1	47	260 gr	1626	3310	1590	352 ± 74
2	47	288 gr	1622	3120	1486	378 ± 77
3	54	368 gr	1636	3309	1503	433 ± 99

C. Improvement of Image Quality

Fig. 5 shows the Doppler images of the three rats, for NC, LC, and FC. Vessels appear sharper and with higher intensity in FC compared with LC and NC, and blurry vessels are resolved after correction. In the FC images, there are dark areas on the sides of the images, which originate from the limited lateral extent of the segmentation.

Fig. 6 shows a quantitative analysis of the resolution improvement in the cortex due to aberration correction. Fig. 6(d) shows that the full correction allows to individually resolve more vessels in the cortex, compared to no correction and lens correction. This finding was consistent for all three rats. In addition to resolving more vessels, Fig. 6(e) shows that vessel width (width at −2-dB level) decreases in LC and FC, indicating an improvement in lateral resolution. For rat 1, the median vessel width was 239.7 μm for NC, 213.2 μm for LC, and 155.7 μm for FC. For rat 2, the median vessel width was 217.5 μm for NC, 224.0 μm for LC, and 162.6 μm for FC. For rat 3, the median vessel width was 256.5 μm for NC, 208.7 μm for LC, and 149.7 μm for FC. On average, the improvement in vessel width was 9% for LC and 32% for FC.

Fig. 7 shows the improvement of the aberration correction method as a function of imaging depth. Fig. 7(b) shows the aberration law for three different depths in the image, corresponding to the cortex, midbrain, and deep brain, and both brain hemispheres. It becomes clear that the aberration is the strongest for the ROI closest to the aberrating layer, and decreases with imaging depth. The maximum time difference of the aberration law is $\approx$1.15 μs, which corresponds to approximately 16 ultrasound periods at 13.9 MHz. Fig. 7(c)

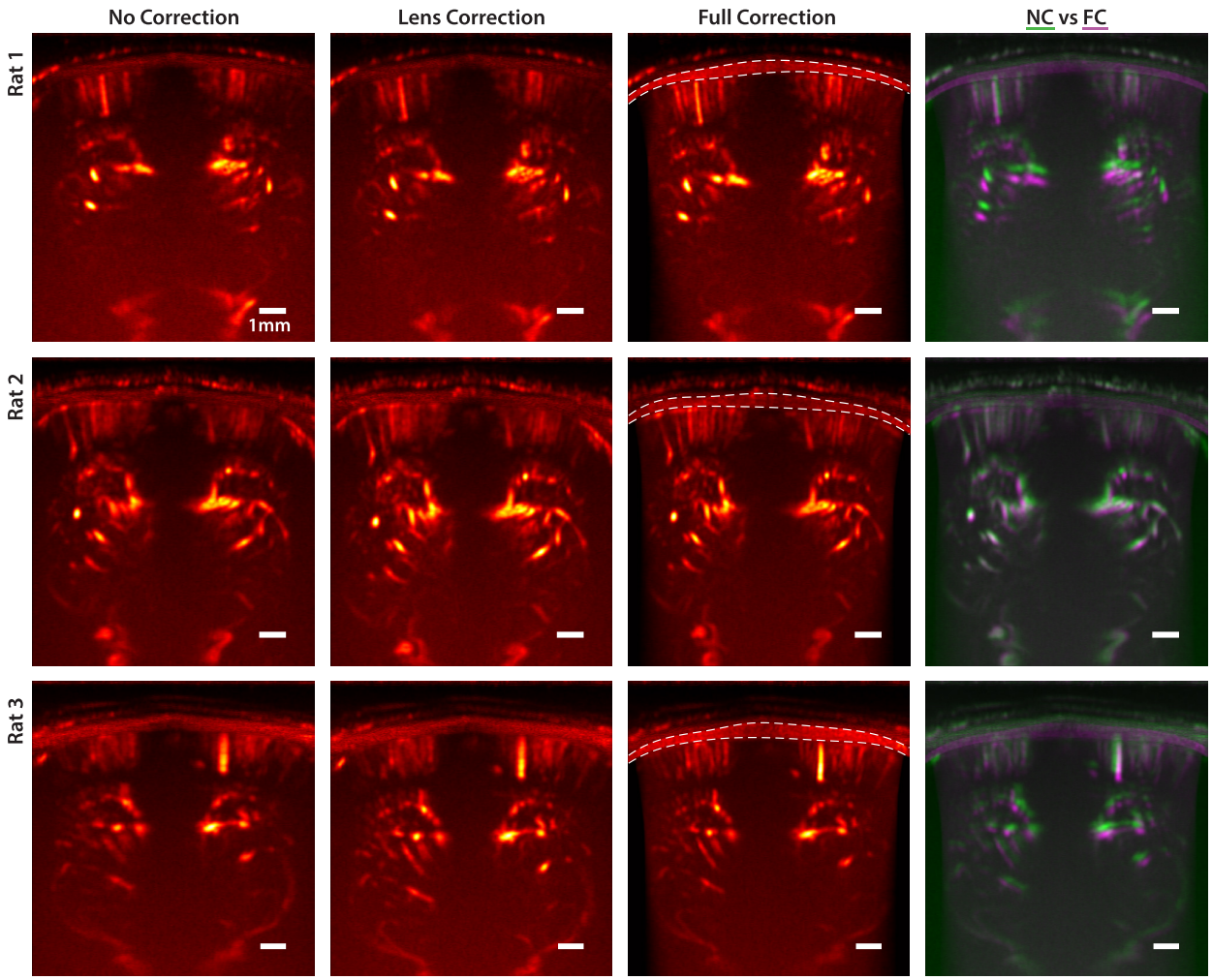

Fig. 5. Power Doppler ultrasound images of three living rat brains. First column the uncorrected image using conventional DAS. The second column shows the lens aberration-corrected image using the two-layer model. The third column shows the fully corrected image using the four-layer model. The last column shows an overlay of the uncorrected image (NC in green) and the fully corrected (FC in magenta) image, created with the MATLAB function `imshowpair`. All scale bars denote 1 mm.

and (d) shows the relative improvement in magnitude and sharpness of the power Doppler image for the three ROIs at different depths. The relative magnitude improvement for LC was 1.3 in the cortex, 1.5 in the midbrain, and 1.4 in the deep brain. For FC, the relative magnitude improvement was 2.1 in the cortex, 1.8 in the midbrain, and 1.6 in the deep brain. The relative sharpness improvement for LC was 3.9 in the cortex, 8.2 in the midbrain, and 4.5 in the deep brain. For FC, the relative sharpness improvement was 31.8 in the cortex, 19.8 in the midbrain, and 8.4 in the deep brain. The improvement in magnitude and sharpness of the FC power Doppler image is highest for the cortex, and decreases with imaging depth. The improvement in FC is higher than in LC for all ROIs and depths.

IV. Discussion

A. Estimation of Tissue Wave Speed and Skull Thickness

In this study, we report an adaptive four-layer ray-tracing method approach to correct skull aberrations in transcranial ultrasound imaging of the adult rat brain. We first validated on a phantom experiment with an aberrating layer having a known thickness and a known wave speed in water. The wave speed in water was estimated with a relative error equal or better than 0.56%. The wave speed found for the PVC layer is in line with the reported values in [67], and the estimated thickness retrieved by segmenting the PVC layer in the B-mode is within the error margin of the caliper measurement (± 10 μm).

The estimated wave speed in the gel/skin layer and the bone layer was in agreement with [50] and [52]. The variability in wave speed may originate from subject variability in age, diet, or experimental conditions such as the probe-skull angle and the fact that the inner and outer skull surface may not be perfectly parallel, reducing specular reflection. The skull thickness retrieved from the aberration-corrected SA images matched well with earlier reports on body mass and skull thickness in rats [54]. For the brain, the estimated wave speeds showed a larger standard deviation, but were still in line with expected values from the literature.

For reliable wave-speed estimation, the ROI should not contain multiple reflections, as these echoes follow different propagation paths than the primary reflections and can bias the result. We therefore recommend selecting an ROI free of mul-

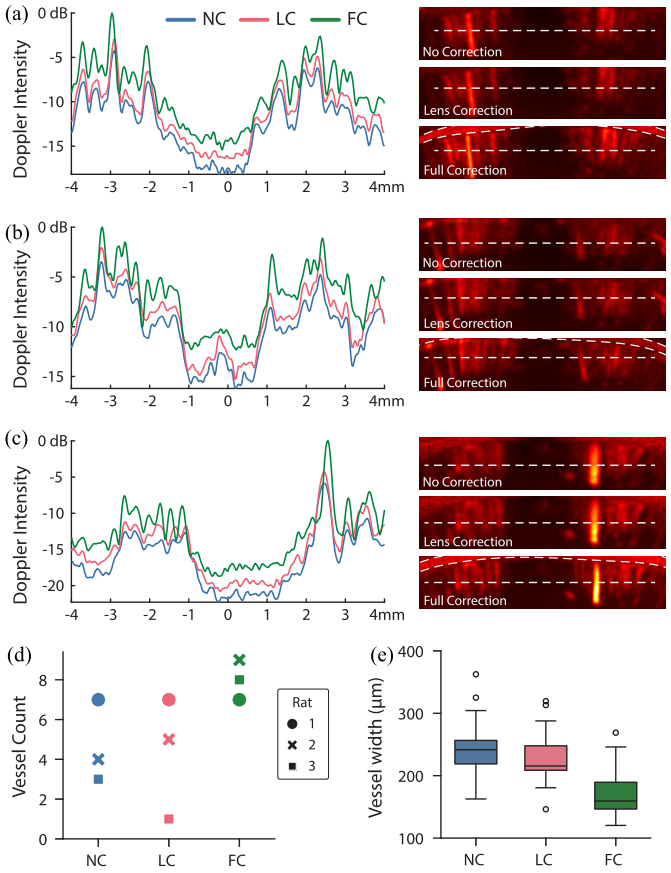

Fig. 6. Power Doppler profiles through the cortex, of (a) rat 1, (b) rat 2, and (c) rat 3. Colors indicate the different reconstruction approaches, with in blue NC, in red LC, and in green FC. The profile corresponds to the white dashed line overlaid on the cortex zoomed-in view on the right of the profiles. (d) Vessel count for the three reconstruction approaches. The vessel count is obtained by identifying peaks in the Doppler intensity profile with a minimum prominence of 2-dB relative to adjacent local minima. (e) Vessel width, defined as the width at the −2-dB level for peaks found in the power Doppler image. The box plots show the combined data of the three rats.

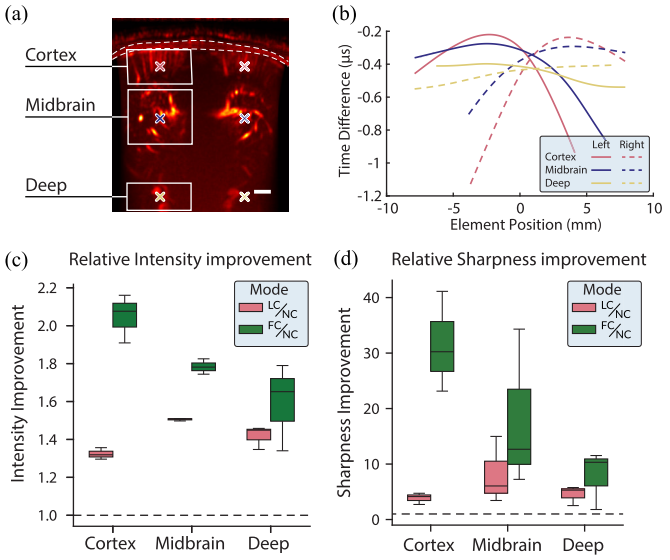

Fig. 7. Aberration correction performance across depth. (a) Three ROIs at different depths in the image, corresponding to the cortex, the midbrain, and deep. The scale bar denotes 1 mm. (b) Aberration law for three different depths (colors correspond to the markers' colors in (a)). Solid lines denote the left hemisphere and the dashed lines the right hemisphere. The aberration law is found by the difference in return time of flight between the full correction and no correction travel time lookup tables. (c) Relative improvement in magnitude of the LC and FC power Doppler images, with respect to NC for the three ROIs at different depths. The black dashed line at 1.0 indicates no improvement. (d) Relative improvement in the Doppler sharpness for three ROIs at different depths of LC and FC with respect to NC.

tiple reflections when autofocusing on B-mode images. In the in vivo experiment, wave-speed estimation was performed on power Doppler images. In this case, the SVD filter suppresses multiple reflections because of their spatiotemporal coherence, and the bias observed in the phantom measurements did not occur. Consequently, the choice of ROI was less critical for the brain wave-speed estimation.

B. Aberration Correction Performance

Evaluating the impact of aberration correction as function of imaging depth showed that the correction performed best in the cortex, as evidenced by magnitude profiles of the power Doppler image through the cortex (see Fig. 6), along with the magnitude and sharpness ratios of the power Doppler images [see Fig. 7(c) and (d)]. For all imaging depths, both the FC and LC methods outperformed the NC approach. As imaging depth increased, the performance of FC became closer to that of LC. This trend can be explained by the nature of aberrations, which are the strongest near the aberrating layer where the incident angles are steepest. This observation aligns with the aberration law shown in Fig. 7(b), which demonstrates that as depth increases, the aberration law flattens.

The flattening of the aberration law explains why the performance difference between LC and FC diminishes with depth. Closer to the aberrating layer, the aberration law also reveals that it is not possible during ray-tracing to find a path to all receiving elements (indicated by the pink lines in Fig. 7(b) that do not span the full lateral field of view). This is caused by steep incident angles at the bone interface, which lead to critical reflection, as shown in Fig. 1(b). For deeper regions, the incident angles at the bone interface decrease, and the ray-tracer successfully can find a path for all receiving elements. Another reason why aberration correction is more effective in the cortex is that here the incident angles to the surface are larger, leading to more pronounced refraction effects, longer paths through the skull, and thus stronger aberrations. In deeper regions, the incident angles are smaller, leading to less pronounced aberrations.

We observed dark patches on the side of the image in the fully aberration-corrected power Doppler images (see Fig. 5). These originate from the ray-tracing process, where for some pixel-transmit combinations, no valid ray path could be found. This occurs when the incident angle at the skull surface exceeds the critical angle, which happens more frequently on the sides due to the curvature of the skull. In other cases, this was caused by the limited lateral extend of the segmentation. As a result, for some pixels, no valid transmit existed, leading to dark patches in the final image. To mitigate this issue, future

implementations could incorporate extrapolation of the skull segmentation beyond the imaged region.

Although the in vivo results show improved vascular contrast, a direct comparison to ground truth remains challenging. Matching the same imaging plane before and after a craniotomy is difficult due to the orthogonal probe orientation, and removing the skull alters intracranial pressure, causing the brain to shift. These effects prevent reliable one-to-one comparison and likewise limit in vivo benchmarking against other aberration correction methods. A possible solution for future work is the recent development of chemical gels that render the skull acoustically transparent without disturbing intracranial pressure [68]. This approach would allow acquisition of a true ground truth image and enable comparison of aberration correction strategies.

C. Challenges in Skull Segmentation and Alignment Between Transducer and Skull

The main challenge of the aberration correction method introduced in this article lies in skull segmentation. For young animals with very thin skulls, the axial resolution of the imaging system can become insufficient and prevent the accurate delineation of the outer and inner skull interfaces. For example, our validation experiment demonstrated that a 300-μm aberrating layer could be resolved using a 1-cycle imaging pulse at 15 MHz, but the 3-cycle-long PW Doppler sequence had an insufficient resolution to detect outer and inner interfaces of the PVC layer. This highlights the need for a high-resolution sequence for skull segmentation. In the current implementation, the axial resolution of our imaging system allows imaging of rats weighing 200 g or more approximately [54].

The accuracy of the skull segmentation also depends on obtaining clear specular reflections from both the outer and inner surfaces of the bone. The outer specular reflection could be reliably obtained during the in vivo data acquisition by verifying with live imaging. However, achieving a clear specular reflection from the inner surface proved challenging due to the absence of an aberration-corrected preview. Obtaining a specular reflection from the inner skull surface is even more challenging when the skull surfaces in the imaging plane are not parallel.

Implementing the method in 3-D using a 2-D matrix array would offer significant advantages. In 3-D imaging, the requirement for precise probe positioning to acquire specular reflections is virtually eliminated. Furthermore, 3-D imaging allows imaging of the brain below nonparallel skull surfaces.

D. Implications for Transcranial Functional Imaging

The advancements presented in this study have significant implications for 2-D fUS. A remaining challenge in 2-D transcranial fUS is navigating to brain ROIs. The requirement of positioning the probe perpendicular to the skull, often results in a power Doppler image of the brain that differs significantly from the standard brain atlas.

One key advantage of our method is the ability to retrieve the wave-speed model once and apply it across any other acquisition sequence. After initialization, functional recordings can be aberration corrected at no additional computational cost, provided that the transducer stays in place.

Our method improves the reconstruction accuracy to show brain regions at the correct anatomical locations and with the correct shape, thus facilitating accurate comparisons with anatomical and functional data from other imaging modalities. Furthermore, enhanced spatial resolution in cortical regions substantially improves the spatial specificity of the fUS signal, improving the usability of transcranial fUS in functional connectomics [69].

Our improved resolution in the cortex would make fUS more sensitive to weak and or transient neural activity. For instance, to create accurate somatotopic mappings during whisker stimulation experiments. The barrelfield is located in the primary somatosensory cortex and contains distinct neuronal clusters, known as barrels, which correspond one-to-one with the whiskers on the rat's face. With interbarrel distances of approximately 50–100 μm, our enhanced resolution would allow the detection of single-whisker activations [70]. Similarly, our method could achieve higher resolution retinotopic mappings of the visual system [71] and tonotopic mappings of the auditory system [72].

To fully unlock the potential of noninvasive fUS and overcome the current limitations of this study, future efforts will focus on extending our aberration correction method to 3-D imaging. This advancement would enable 4-D transcranial imaging, offering comprehensive spatiotemporal resolution and further advancing the utility of fUS in neuroscience.

V. Conclusion

We developed an adaptive aberration correction method using four-layer ray-tracing that can improve image quality and signal spatial specificity in transcranial ultrasound Doppler imaging of the adult rat brain. The method adapts to each subject and each brain section being imaged without requiring prior information from additional imaging modalities like a CT or MRI scan. The method consistently outperformed conventional DAS image reconstruction and holds promise for functional imaging applications that require high spatial sensitivity.

Acknowledgment

The authors thank Ruud van Tol (NIN, KNAW) for designing the ultrasound probe holder, Henry den Bok (ImPhys, TU Delft) for fabricating wire phantoms, Ronald Ligteringen (ImPhys, TU Delft) for facilitating access to computational resources, and Gert Jan de Fluiter (NIN, KNAW) for his assistance with animal care.

Rick Waasdorp, Eleonora Muñoz-Ibarra, David Maresca, and Guillaume Renaud are with the Laboratory of Medical Imaging, Department of Imaging Physics, Delft University of Technology, 2628 CJ Delft, The Netherlands (e-mail: d.maresca@tudelft.nl; g.g.j.renaud@tudelft.nl).

Flora Nelissen and Valeria Gazzola are with the Social Brain Laboratory, Netherlands Institute for Neuroscience, 1105 BA Amsterdam, The Netherlands.

Baptiste Heiles was with Delft University of Technology, 2628 CJ Delft, The Netherlands. He is now with the Division of Chemistry and

Chemical Engineering, California Institute of Technology, Pasadena, CA 91125 USA.

REFERENCES

[1] É. Macé, G. Montaldo, I. Cohen, M. Baulac, M. Fink, and M. Tanter, "Functional ultrasound imaging of the brain," *Nature Methods*, vol. 8, no. 8, pp. 662–664, Aug. 2011.

[2] A. O. Nunez-Elizalde et al., "Neural correlates of blood flow measured by ultrasound," *Neuron*, vol. 110, no. 10, pp. 1631–1640, May 2022.

[3] T. Deffieux, C. Demené, and M. Tanter, "Functional ultrasound imaging: A new imaging modality for neuroscience," *Neuroscience*, vol. 474, pp. 110–121, Oct. 2021.

[4] C. Demene et al., "Functional ultrasound imaging of brain activity in human newborns," *Sci. Translational Med.*, vol. 9, no. 411, p. 6756, Oct. 2017.

[5] M. Imbault, D. Chauvet, J.-L. Gennisson, L. Capelle, and M. Tanter, "Intraoperative functional ultrasound imaging of human brain activity," *Sci. Rep.*, vol. 7, no. 1, p. 7304, Aug. 2017.

[6] S. Soloukey et al., "Functional imaging of the exposed brain," *Frontiers Neurosci.*, vol. 17, Feb. 2023, Art. no. 1087912.

[7] S. Soloukey et al., "Functional ultrasound (fUS) during awake brain surgery: The clinical potential of intra-operative functional and vascular brain mapping," *Frontiers Neurosci.*, vol. 13, Jan. 2020, Art. no. 1384.

[8] A. Dizeux et al., "Functional ultrasound imaging of the brain reveals propagation of task-related brain activity in behaving primates," *Nature Commun.*, vol. 10, no. 1, p. 1400, Mar. 2019.

[9] S. L. Norman et al., "Single-trial decoding of movement intentions using functional ultrasound neuroimaging," *Neuron*, vol. 109, no. 9, pp. 1554–1566, May 2021.

[10] D. A. Hernandez, V. H. Contreras, L. Leija, A. Vera, D. Martinez-Fong, and M. I. Gutierrez, "Acoustic field simulation for focused ultrasound on skull with craniotomy for drug delivery in rat brain," in *Proc. Global Med. Eng. Phys. Exchanges/Pan Amer. Health Care Exchanges (GMEPE/PAHCE)*, Mar. 2017, pp. 1–5.

[11] B. Lucht, A. Hubbell, and K. Hynynen, "Contrast-enhanced transcranial two-dimensional ultrasound imaging using shear-mode conversion at low frequency," *Ultrasound Med. Biol.*, vol. 39, no. 2, pp. 332–344, Feb. 2013.

[12] G. Pinton, J.-F. Aubry, E. Bossy, M. Müller, M. Pernot, and M. Tanter, "Attenuation, scattering, and absorption of ultrasound in the skull bone," *Med. Phys.*, vol. 39, no. 1, pp. 299–307, Dec. 2011.

[13] B. D. Lindsey and S. W. Smith, "Refraction correction in 3D transcranial ultrasound imaging," *Ultrason. Imag.*, vol. 36, no. 1, pp. 35–54, Jan. 2014.

[14] C. Rabut et al., "Functional ultrasound imaging of human brain activity through an acoustically transparent cranial window," *Sci. Transl. Med.*, vol. 16, no. 749, p. 3143, May 2024.

[15] E. Tiran et al., "Transcranial functional ultrasound imaging in freely moving awake mice and anesthetized young rats without contrast agent," *Ultrasound Med. Biol.*, vol. 43, no. 8, pp. 1679–1689, Aug. 2017.

[16] A. Bertolo et al., "High sensitivity mapping of brain-wide functional networks in awake mice using simultaneous multi-slice fUS imaging," *Imag. Neurosci.*, vol. 1, pp. 1–18, Nov. 2023.

[17] M. Li et al., "Age-related changes of material mechanics and bone material parameters of rat skulls," *Fa Yi Xue Za Zhi*, vol. 37, no. 1, pp. 1–6, Feb. 2021.

[18] A. Urban, E. Mace, C. Brunner, M. Heidmann, J. Rossier, and G. Montaldo, "Chronic assessment of cerebral hemodynamics during rat forepaw electrical stimulation using functional ultrasound imaging," *NeuroImage*, vol. 101, pp. 138–149, Nov. 2014.

[19] C. Errico, B.-F. Osmanski, S. Pezet, O. Couture, Z. Lenkei, and M. Tanter, "Transcranial functional ultrasound imaging of the brain using microbubble-enhanced ultrasensitive Doppler," *NeuroImage*, vol. 124, pp. 752–761, Jan. 2016.

[20] D. Maresca et al., "Acoustic biomolecules enhance hemodynamic functional ultrasound imaging of neural activity," *NeuroImage*, vol. 209, Apr. 2020, Art. no. 116467.

[21] R. Ali et al., "Aberration correction in diagnostic ultrasound: A review of the prior field and current directions," *Zeitschrift für Medizinische Physik*, vol. 33, no. 3, pp. 267–291, Aug. 2023.

[22] R. Mallart and M. Fink, "Adaptive focusing in scattering media through sound-speed inhomogeneities: The van Cittert Zernike approach and focusing criterion," *J. Acoust. Soc. Amer.*, vol. 96, no. 6, pp. 3721–3732, Dec. 1994.

[23] S. W. Flax and M. O'Donnell, "Phase-aberration correction using signals from point reflectors and diffuse scatterers: Basic principles," *IEEE Trans. Ultrason. Ferroelectr., Freq. Control*, vol. 35, no. 6, pp. 758–767, Nov. 1988.

[24] L. Nock, G. E. Trahey, and S. W. Smith, "Phase aberration correction in medical ultrasound using speckle brightness as a quality factor," *J. Acoust. Soc. Amer.*, vol. 85, no. 5, pp. 1819–1833, May 1989.

[25] J. Robin et al., "In vivo adaptive focusing for clinical contrast-enhanced transcranial ultrasound imaging in human," *Phys. Med. Biol.*, vol. 68, no. 2, Jan. 2023, Art. no. 025019.

[26] N. M. Ivancevich, G. F. Pinton, H. A. Nicoletto, E. Bennett, D. T. Laskowitz, and S. W. Smith, "Real-time 3-D contrast-enhanced transcranial ultrasound and aberration correction," *Ultrasound Med. Biol.*, vol. 34, no. 9, pp. 1387–1395, Sep. 2008.

[27] D. E. Soulioti, D. Espíndola, P. A. Dayton, and G. F. Pinton, "Super-resolution imaging through the human skull," *IEEE Trans. Ultrason., Ferroelectr., Freq. Control*, vol. 67, no. 1, pp. 25–36, Jan. 2020.

[28] N. M. Ivancevich, J. J. Dahl, G. E. Trahey, and S. W. Smith, "Phase-aberration correction with a 3-D ultrasound scanner: Feasibility study," *IEEE Trans. Ultrason., Ferroelectr., Freq. Control*, vol. 53, no. 8, pp. 1432–1439, Aug. 2006.

[29] M. Mozaffarzadeh, M. D. Verweij, N. de Jong, and G. Renaud, "Comparison of phase-screen and geometry-based phase aberration correction techniques for real-time transcranial ultrasound imaging," *Appl. Sci.*, vol. 12, no. 19, p. 10183, Oct. 2022.

[30] R. Ali, T. Brevett, D. Hyun, L. L. Brickson, and J. J. Dahl, "Distributed aberration correction techniques based on tomographic sound speed estimates," *IEEE Trans. Ultrason., Ferroelectr., Freq. Control*, vol. 69, no. 5, pp. 1714–1726, May 2022.

[31] M. Jaeger, E. Robinson, H. G. Akarçay, and M. Frenz, "Full correction for spatially distributed speed-of-sound in echo ultrasound based on measuring aberration delays via transmit beam steering," *Phys. Med. Biol.*, vol. 60, no. 11, pp. 4497–4515, May 2015.

[32] R. Ali et al., "Sound speed estimation for distributed aberration correction in laterally varying media," *IEEE Trans. Comput. Imag.*, vol. 9, pp. 367–382, 2023.

[33] F. Bureau, J. Robin, A. Le Ber, W. Lambert, M. Fink, and A. Aubry, "Three-dimensional ultrasound matrix imaging," *Nature Commun.*, vol. 14, no. 1, p. 6793, Oct. 2023.

[34] F. Bureau, L. Denis, A. Coudert, M. Fink, O. Couture, and A. Aubry, "Ultrasound matrix imaging for 3D transcranial in vivo localization microscopy," *Sci. Adv.*, vol. 11, no. 31, Jul. 2025, Art. no. eadt9778.

[35] P. Xing et al., "Phase aberration correction for in vivo ultrasound localization microscopy using a spatiotemporal complex-valued neural network," *IEEE Trans. Med. Imag.*, vol. 43, no. 2, pp. 662–673, Feb. 2024.

[36] M. Sharifzadeh, S. Goudarzi, A. Tang, H. Benali, and H. Rivaz, "Mitigating aberration-induced noise: A deep learning-based aberration-to- aberration approach," *IEEE Trans. Med. Imag.*, vol. 43, no. 12, pp. 4380–4392, Dec. 2024.

[37] M. Mozaffarzadeh, E. Verschuur, M. D. Verweij, V. Daeichin, N. De Jong, and G. Renaud, "Refraction-corrected transcranial ultrasound imaging through the human temporal window using a single probe," *IEEE Trans. Ultrason., Ferroelectr., Freq. Control*, vol. 69, no. 4, pp. 1191–1203, Apr. 2022.

[38] G. Renaud, P. Kruizinga, D. Cassereau, and P. Laugier, "In vivo ultrasound imaging of the bone cortex," *Phys. Med. Biol.*, vol. 63, no. 12, Jun. 2018, Art. no. 125010.

[39] G. Renaud, P. Clouzet, D. Cassereau, and M. Talmant, "Measuring anisotropy of elastic wave velocity with ultrasound imaging and an autofocus method: Application to cortical bone," *Phys. Med. Biol.*, vol. 65, no. 23, Nov. 2020, Art. no. 235016.

[40] J.-F. Aubry, M. Tanter, M. Pernot, J.-L. Thomas, and M. Fink, "Experimental demonstration of noninvasive transskull adaptive focusing based on prior computed tomography scans," *J. Acoust. Soc. Amer.*, vol. 113, no. 1, pp. 84–93, Jan. 2003.

[41] C. Jiang, Y. Li, K. Xu, and D. Ta, "Full-matrix phase shift migration method for transcranial ultrasonic imaging," *IEEE Trans. Ultrason., Ferroelectr., Freq. Control*, vol. 68, no. 1, pp. 72–83, Jan. 2021.

[42] T. Wang and Y. Jing, "Transcranial ultrasound imaging with speed of sound-based phase correction: A numerical study," *Phys. Med. Biol.*, vol. 58, no. 19, pp. 6663–6681, Sep. 2013.

[43] J. A. Sethian, "Fast marching methods," *SIAM Rev.*, vol. 41, no. 2, pp. 199–235, Jan. 1999.

[44] J. Zhou et al., "Transcranial ultrafast ultrasound Doppler imaging: A phantom study," *Ultrasonics*, vol. 144, Dec. 2024, Art. no. 107430.

[45] C. Jiang et al., "Ray theory-based compounded plane wave ultrasound imaging for aberration corrected transcranial imaging: Phantom experiments and simulations," *Ultrasonics*, vol. 135, Dec. 2023, Art. no. 107124.

[46] M. Mozaffarzadeh, D. J. E. Verschuur, M. D. Verweij, N. de Jong, and G. Renaud, "Accelerated 2-D real-time refraction-corrected transcranial ultrasound imaging," *IEEE Trans. Ultrason., Ferroelectr., Freq. Control*, vol. 69, no. 9, pp. 2599–2610, Sep. 2022.

[47] D. A. Waltham, "Two-point ray tracing using Fermat's principle," *Geophys. J. Int.*, vol. 93, no. 3, pp. 575–582, Jun. 1988.

[48] V. Perrot, M. Polichetti, F. Varray, and D. Garcia, "So you think you can DAS? A viewpoint on delay-and-sum beamforming," *Ultrasonics*, vol. 111, Mar. 2021, Art. no. 106309.

[49] R. Waasdorp, D. Maresca, and G. Renaud, "Assessing transducer parameters for accurate medium sound speed estimation and image reconstruction," *IEEE Trans. Ultrason., Ferroelectr., Freq. Control*, vol. 71, no. 10, pp. 1233–1243, Oct. 2024.

[50] T. D. Mast, "Empirical relationships between acoustic parameters in human soft tissues," *Acoust. Res. Lett. Online*, vol. 1, no. 2, pp. 37–42, Oct. 2000.

[51] P. Harris and R. Petherick, "Ultrasonic transmission and reflection measurements of a rat skull," in *Proc. 9th Int. Conf. Sens. Technol. (ICST)*, Dec. 2015, pp. 822–827.

[52] M. A. O'Reilly, A. Müller, and K. Hynynen, "Ultrasound insertion loss of rat parietal bone appears to be proportional to animal mass at submegahertz frequencies," *Ultrasound Med. Biol.*, vol. 37, no. 11, pp. 1930–1937, Nov. 2011.

[53] M. A. Aydin, M. S. Kilinc, A. S. Ergun, A. Bozkurt, and E. Deveci, "Ultrasonic transmittance of rat skull as a function of frequency," in *Proc. IEEE Int. Ultrason. Symp. (IUS)*, Sep. 2016, pp. 1–4.

[54] M. Gerstenmayer, B. Fellah, R. Magnin, E. Selingue, and B. Larrat, "Acoustic transmission factor through the rat skull as a function of body mass, frequency and position," *Ultrasound Med. Biol.*, vol. 44, no. 11, pp. 2336–2344, Nov. 2018.

[55] F. Zhu, "Development of an FE model of the rat head subjected to air shock loading," in *Proc. 54th Stapp Car Crash Conf.*, Nov. 2010, p. 22.

[56] H. Mao, C. Wagner, F. Guan, Y. N. Yeni, and K. H. Yang, "Material properties of adult rat skull," *J. Mech. Med. Biol.*, vol. 11, no. 5, pp. 1199–1212, Dec. 2011.

[57] R. L. Nasoni, T. Bowen, W. G. Connor, and R. R. Sholes, "In vivo temperature dependence of ultrasound speed in tissue and its application to noninvasive temperature monitoring," *Ultrasonic Imag.*, vol. 1, no. 1, pp. 34–43, Jan. 1979.

[58] T. Bowen, W. G. Connor, R. L. Nasoni, A. E. Pifer, and R. R. Sholes, "Measurement of the temperature dependence of the velocity of ultrasound in soft tissues," *Ultrason. Tissue Charact. II*, vol. 525, pp. 57–61, Aug. 1979.

[59] R. P. Brent, *Algorithms for Minimization Without Derivatives*. Upper Saddle River, NJ, USA: Prentice-Hall, 1973.

[60] A. R. Selfridge, G. S. Kino, and B. T. Khuri-Yakub, "A theory for the radiation pattern of a narrow-strip acoustic transducer," *Appl. Phys. Lett.*, vol. 37, no. 1, pp. 35–36, Jul. 1980.

[61] R. Wituła and D. Słota, "Cardano's formula, square roots, Chebyshev polynomials and radicals," *J. Math. Anal. Appl.*, vol. 363, no. 2, pp. 639–647, Mar. 2010.

[62] B. E. Treeby, T. K. Varslot, E. Z. Zhang, J. G. Laufer, and P. C. Beard, "Automatic sound speed selection in photoacoustic image reconstruction using an autofocus approach," *J. Biomed. Opt.*, vol. 16, no. 9, Sep. 2011, Art. no. 090501.

[63] W. Marczak, "Water as a standard in the measurements of speed of sound in liquids," *J. Acoust. Soc. Amer.*, vol. 102, no. 5, pp. 2776–2779, Nov. 1997.

[64] J. A. Jensen, S. I. Nikolov, K. L. Gammelmark, and M. H. Pedersen, "Synthetic aperture ultrasound imaging," *Ultrason.*, vol. 44, pp. e5–e15, Dec. 2006.

[65] G. Montaldo, M. Tanter, J. Bercoff, N. Benech, and M. Fink, "Coherent plane-wave compounding for very high frame rate ultrasonography and transient elastography," *IEEE Trans. Ultrason., Ferroelectr., Freq. Control*, vol. 56, no. 3, pp. 489–506, Mar. 2009.

[66] C. Demené et al., "Spatiotemporal clutter filtering of ultrafast ultrasound data highly increases Doppler and fUltrasound sensitivity," *IEEE Trans. Med. Imag.*, vol. 34, no. 11, pp. 2271–2285, Nov. 2015.

[67] A. R. Selfridge, "Approximate material properties in isotropic materials," *IEEE Trans. Sonics Ultrason.*, vol. SU-32, no. 3, pp. 381–394, May 1985.

[68] Z. Wang et al., "Acoustic transparency enabling functional ultrasound imaging through mouse and human skulls," *BioRxiv*, Aug. 2025.

[69] J. M. M. de Paz and E. Macé, "Functional ultrasound imaging: A useful tool for functional connectomics?" *NeuroImage*, vol. 245, Dec. 2021, Art. no. 118722.

[70] K. Tripathi, T. Zhang, N. McDannold, Y.-Z. Zhang, G. Ehnholm, and Y. Okada, "Direct activation of cortical neurons in the primary somatosensory cortex of the rat in vivo using focused ultrasound," *Ultrasound Med. Biol.*, vol. 46, no. 9, pp. 2349–2360, Sep. 2020.

[71] É. Macé et al., "Whole-brain functional ultrasound imaging reveals brain modules for visuomotor integration," *Neuron*, vol. 100, no. 5, pp. 1241–1251, Dec. 2018.

[72] C. Bimbard et al., "Multi-scale mapping along the auditory hierarchy using high-resolution functional UltraSound in the awake ferret," *ELife*, vol. 7, p. 35028, Jun. 2018.